

# Microstructure and electronic properties of the refractory semiconductor ScN grown on MgO(001) by ultra-high-vacuum reactive magnetron sputter deposition

D. Gall and I. Petrov<sup>a)</sup>

Materials Science Department, Coordinated Science Laboratory, and Materials Research Laboratory,  
University of Illinois, Urbana, Illinois 61801

L. D. Madsen

Materials Science Department, Coordinated Science Laboratory, and Materials Research Laboratory,  
University of Illinois, Urbana, Illinois 61801  
and Thin Film Division, Physics Department, Linköping University, S-581 83 Linköping, Sweden

J.-E. Sundgren

Thin Film Division, Physics Department, Linköping University, S-581 83 Linköping, Sweden

J. E. Greene

Materials Science Department, Coordinated Science Laboratory, and Materials Research Laboratory,  
University of Illinois, Urbana, Illinois 61801  
and Thin Film Division, Physics Department, Linköping University, S-581 83 Linköping, Sweden

(Received 24 September 1997; accepted 13 March 1998)

ScN layers, 180 nm thick, were grown on MgO(001) substrates at 750 °C by ultra-high-vacuum reactive magnetron sputter deposition in pure N<sub>2</sub> discharges. N/Sc ratios, determined by Rutherford backscattering spectroscopy, were  $0.98 \pm 0.02$ . X-ray diffraction  $\theta$ - $2\theta$  scans and pole figures combined with plan-view and cross-sectional transmission electron microscopy showed that the films are strongly textured, both in plane and along the growth direction, and have a columnar microstructure with an average column width near the film surface of  $30 \pm 5$  nm. During nucleation and the early stages of film growth, the layers consist of approximately equal volume fractions of 002- and 111-oriented grains. However, preferred orientation evolves toward a purely 111 texture within  $\approx 40$  nm as the 002 grains grow out of existence in a kinetically limited competitive growth mode. 002 grains exhibit local cube-on-cube epitaxy with an orientation relationship  $(001)_{\text{ScN}} \parallel (001)_{\text{MgO}}$  and  $[010]_{\text{ScN}} \parallel [010]_{\text{MgO}}$  while 111 grains have a complex fourfold 90°-rotated in-plane preferred orientation in which strained ScN triangular {111} surface unit cells exhibit local epitaxy with square MgO unit cells yielding the orientation relationship  $(111)_{\text{ScN}} \parallel (001)_{\text{MgO}}$ ,  $[1\bar{1}0]_{\text{ScN}} \parallel [1\bar{1}0]_{\text{MgO}}$ , and  $[11\bar{2}]_{\text{ScN}} \parallel [110]_{\text{MgO}}$ . Room-temperature electrical resistivity  $\rho$  is  $1.2 \times 10^4 \mu\Omega \text{ cm}$  while  $d\rho/dT$  was found to be negative, indicating semiconducting behavior, with  $\rho$  varying from  $1.6 \times 10^4 \mu\Omega \text{ cm}$  at 80 K to  $1.1 \times 10^4 \mu\Omega \text{ cm}$  at 400 K. Optical absorption coefficients ranged from  $1 \times 10^4 \text{ cm}^{-1}$  at 1.5 eV to  $2.6 \times 10^5 \text{ cm}^{-1}$  at 3.5 eV with a well-defined edge corresponding to a direct transition at  $2.37 \pm 0.05$  eV. © 1998 American Vacuum Society. [S0734-2101(98)07704-5]

## I. INTRODUCTION

Transition-metal nitrides are well known for their remarkable physical properties including high hardness and mechanical strength, chemical inertness, and electrical resistivities that vary from metallic to semiconducting. As a result, they are widely studied and have become technologically important for applications such as hard wear-resistant coatings, diffusion barriers, and optical coatings. While TiN has received by far the most attention and is presently used commercially in all of the above-mentioned applications, the neighboring nitride on the periodic table, ScN, is almost totally unexplored. Like TiN, which is stable over a composition range N/Ti=0.6–1,<sup>1</sup> we expect that NaCl-structure ScN will have a large single-phase field.

TiN is a B-1 NaCl structure IVB–V compound with an electronic structure characterized by partially overlapping N 2*p* and Ti 3*d* bands.<sup>1</sup> Stoichiometric TiN exhibits a pronounced density-of-states (DOS) minimum at an energy just less than the Fermi-level  $E_f$ . Since each TiN formula unit has nine valence electrons, one electron occupies an anti-bonding state above the DOS minimum. Thus, TiN is metallic with a room-temperature resistivity of  $\approx 15 \mu\Omega \text{ cm}$ .<sup>1,2</sup> Sc is a group IIIB metal with one less 3*d* electron than Ti, and therefore, provides ScN with eight valence electrons in the primitive unit cell.  $E_f$  for ScN is, therefore, exactly between the N 2*p* and Sc 3*d* bands. Available band-structure calculations are not sufficiently accurate to conclude whether or not there is band overlap in the ScN DOS.<sup>3</sup>

The few published data on electronic properties of ScN are contradictory. Self-consistent augmented-plane-wave band-structure calculations by Neckel *et al.*<sup>4</sup> predict a tiny,

<sup>a)</sup>Electronic mail: petrov@uiuc.edu

0.01 eV, overlap of valence bands at the  $\Gamma$  point with conduction bands at the  $X$  point, leading to metallic conductivity. However, the uncertainty in the relative energy positions of the bands in these calculations is 1 eV. Johansson *et al.*<sup>5</sup> compared similar band-structure calculations for TiN with angle-resolved photoelectron spectroscopy data and found significant differences at high symmetry points in the Brillouin zone. The energy of the  $\Delta_5$  valence band at the  $\Gamma$  point was predicted 1 eV too high and the  $\Delta_2'$  conduction band at the  $X$  point was 1 eV too low. In the band-structure calculations for ScN, these two points define the overlap of valence and conduction bands which means that, assuming a similar error in the ScN calculations, ScN could have a band gap of  $\approx 2$  eV.

Dismukes and co-workers<sup>6,7</sup> reported the growth of polycrystalline ScN on  $\alpha$ -Al<sub>2</sub>O<sub>3</sub>(1 $\bar{1}$ 02) by chemical vapor deposition from NH<sub>3</sub> and halides produced by the reaction of HCl, HBr, or HI with Sc. Films, several  $\mu\text{m}$  thick, were grown at 750–1150 °C with a reported N/Sc ratio of  $0.99 \pm 0.01$  as determined by wet chemistry. Hall measurements showed a donor concentration of  $10^{20}$ – $10^{21}$  cm<sup>-3</sup>, which the authors assumed to stem from incorporated halogen impurities. Nevertheless, optical absorption measurements, after subtraction of free-carrier effects, yielded an estimated optical band gap of 2.1 eV. The authors were unable to determine whether the band gap was direct or indirect due to the large exponential tail in the data.

In this article, we present the results of an investigation of the microstructure and electronic properties of polycrystalline ScN films grown by ultra-high-vacuum (UHV) reactive magnetron sputtering in pure N<sub>2</sub> discharges. 180 nm thick layers were deposited on MgO(001) substrates and found to grow with a very strong (111) preferred orientation in the growth direction. They also exhibit a fourfold in-plane preferred orientation in which strained ScN two-dimensional triangular {111} unit cells meshed with square MgO unit cells. The films are nearly stoichiometric with N/Sc =  $0.98 \pm 0.02$ . The microstructure is columnar with an average column size of 30 nm and a relaxed lattice constant of 0.4499 nm. Room-temperature resistivity was found to be  $1.2 \times 10^4$   $\mu\Omega$  cm and to increase with decreasing temperature, indicating semiconducting behavior. Optical transmission and reflection measurements were used to determine absorption coefficients as a function of photon energy. Analysis of the data shows that the ScN layers have a direct optical transition at  $2.37 \pm 0.05$  eV.

## II. EXPERIMENTAL PROCEDURE

All films were grown in a two-chamber turbomolecular-pumped UHV deposition system. The apparatus consists of a sample introduction chamber, which was evacuated to  $5 \times 10^{-8}$  Torr ( $6.7 \times 10^{-6}$  Pa) prior to sample transfer, and a three-target magnetron growth chamber with a base pressure of  $1 \times 10^{-9}$  Torr ( $1.3 \times 10^{-7}$  Pa). The target was a 5 cm diam water-cooled Sc disk, 99.9% pure with the only detectable contaminant being 0.1 at. % Ta, the usual impurity in Sc. Sputtering was carried out in pure N<sub>2</sub> (99.999%), intro-

duced through a high-precision solenoid valve, at 5 mTorr (0.7 Pa). The pressure was measured by a capacitance manometer and maintained constant with an automatic mass-flow controller. A current-regulated dc supply was used to provide a discharge current of 0.5 A and a target voltage of 313 V which, with the target-to-substrate separation of 15 cm, resulted in a film deposition rate of 57 nm h<sup>-1</sup> in the fully target-poisoned regime. The target was sputter etched for 5 min, with a shutter shielding the substrate, prior to initiating deposition.

The substrates were polished  $10 \times 10 \times 1$  mm<sup>3</sup> MgO(001) wafers, which were cleaned and degreased by successive rinses in ultrasonic baths of trichloroethane, acetone, methanol, and deionized water and then blown dry in dry N<sub>2</sub>. They were then mounted on resistively heated Ta platens using a Mo clip and inserted into the sample introduction chamber for transport into the deposition chamber. Final substrate cleaning consisted of thermal degassing at 800 °C for 1 h, a procedure shown to result in sharp MgO(001)  $1 \times 1$  reflection high-energy electron diffraction patterns.<sup>8</sup> Film growth temperature, 750 °C including the contribution due to plasma heating, was measured using a pyrometer calibrated by a thermocouple that was bonded to a dummy MgO wafer. Following deposition, the samples were allowed to cool to  $< 100$  °C before transferring them to the load-lock chamber, which was then vented with dry N<sub>2</sub>.

Film microstructure and texture were investigated using  $\theta$ - $2\theta$  x-ray diffraction (XRD) and XRD pole figures. The former measurements were carried out using Cu  $K\alpha$  radiation with a Ni filter to remove Cu  $K\beta$  reflections, a powder diffractometer scanned over the range 30–130°  $2\theta$  at steps of 0.01°, a 0.5° divergence slit, and a 0.2° receiving slit. Pole figures were obtained using a four-circle Phillips MRD diffractometer. The system was operated at 30 kV and 30 mA with parallel beam x-ray optics, a  $1 \times 1$  mm<sup>2</sup> point-focus Cu x-ray source with a Ni filter, and a  $1 \times 1$  mm<sup>2</sup> collimator slit at a distance of 160 mm from the source. This configuration resulted in 0.35° collimation of the incident beam. The secondary optics consisted of a 0.27° parallel-plate collimator followed by a flat graphite secondary monochromator and a proportional detector. The sample was mounted on an Eulerian cradle with 360° of freedom in the azimuthal angle  $\phi$  and 100°, measured from the normal to the sample diffraction plane, in the tilt angle  $\psi$ . Pole figure data were acquired with 2° steps in  $\psi$  and  $\phi$ .

Plan-view and cross-sectional transmission electron microscopy (TEM and XTEM) analyses were carried out in a Phillips CM12 microscope with a LaB<sub>6</sub> filament operated at 120 kV. Plan-view specimens were prepared by mechanically thinning from the back side with SiC to a thickness of  $\approx 30$   $\mu\text{m}$ . Final thinning to electron transparency was accomplished by ion milling using a 5.5 kV Ar<sup>+</sup>-ion beam incident initially at 14° and then decreased to 12°. Cross-sectional specimens were prepared by gluing two samples film to film and then cutting vertical sections, which were ground and milled similar to the plan-view samples, but from both sides.

The microchemistry of as-deposited films was examined

using a combination of Rutherford backscattering spectroscopy (RBS) and x-ray photoelectron spectroscopy (XPS). The RBS probe beam consisted of 2 MeV  $\text{He}^+$  ions incident at an angle of  $22.5^\circ$  relative to the sample surface normal with the detector set at a  $150^\circ$  scattering angle. Backscattered spectra were analyzed to determine N/Sc ratios using the RUMP simulation program.<sup>9</sup> XPS measurements were carried out in a Perkin–Elmer PHI 5400 spectrometer equipped with a Mg  $K\alpha$  x-ray source and a hemispherical detector. The ScN samples were capped *in situ* with a 20 nm thick TiN layer, grown at  $T_s = 500^\circ\text{C}$ , to prevent air exposure during transfer between the deposition and analysis chambers. The TiN cap layer was removed by  $\text{Ar}^+$  sputter etching using beam rastering over a  $3 \times 3 \text{ mm}^2$  area. Etching was continued until no Ti was detected in the  $1 \text{ mm}^2$  analysis area.

Transmission and reflection spectra were obtained over the range between 300 and 2000 nm using a Perkin–Elmer Lambda 9 spectrophotometer with an integrating sphere for light collection. Spectral intensity distributions were calibrated using reflection spectra from an undoped single-crystal Si(001) wafer. ScN conductivity was measured as a function of temperature between 80 and 400 K using a four-point probe. For this purpose, four Ti/TiN bilayer contacts were sputter deposited in the van der Pauw geometry<sup>10</sup> through a mask.

### III. EXPERIMENTAL RESULTS AND DISCUSSION

ScN films as well as ScN layers capped with 20 nm thick TiN overlayers were analyzed by RBS and found to be nearly stoichiometric with N/Sc ratios  $0.98 \pm 0.02$ . No impurities, other than the 0.1 at. % Ta in the Sc target, were detected by either RBS or XPS.

Figure 1 is a portion of a typical XRD  $\theta$ – $2\theta$  scan, obtained over the  $2\theta$  range from  $30^\circ$  to  $130^\circ$ , showing a strong (111) ScN peak at  $34.415^\circ$  and a much weaker (002) peak at  $39.79^\circ$ . From Ref. 11, the ratio of the 111 to 002 peak intensities for randomly oriented ScN is 0.66 while we obtain a ratio of 19 indicating that the layers have a very strong 111 preferred orientation. The full width at half maximum (FWHM) intensity of the 111 peak is  $0.2^\circ$  while that of the 002 peak is  $0.5^\circ$  corresponding to XRD coherence lengths of 41 and 17 nm, respectively, along the film growth direction.

Reported bulk ScN lattice constants  $a_{\text{ScN}}$  vary from 0.4500 to 0.4505 nm.<sup>11–14</sup> Based upon the 111 (Fig. 1) as well as higher-order 222 and 333 XRD peaks, we obtain a value of 0.4510 nm, which is somewhat larger than previously published values and indicates the presence of in-plane compressive stress. This can be accounted for by differential thermal contraction during cooling from the deposition temperature,  $750^\circ\text{C}$ , to room temperature. The thermal expansion coefficients of ScN and MgO are  $4 \times 10^{-6} \text{ }^\circ\text{C}^{-1}$  (Ref. 12) and  $1.3 \times 10^{-5} \text{ }^\circ\text{C}^{-1}$  (Ref. 15), respectively. While Poisson's ratio  $\nu$  for ScN is unknown,  $\nu$  for neighboring transition-metal nitrides vary from 0.19 for ZrN (Ref. 16) to 0.22 for TiN.<sup>17</sup> Using  $\nu_{\text{ScN}} = 0.22$ – $0.19$ , assuming a biaxial

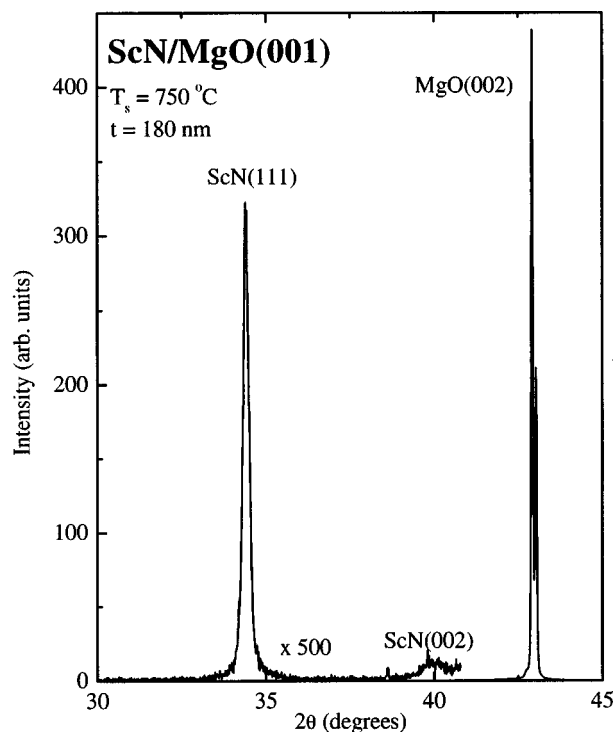


FIG. 1. XRD  $\theta$ – $2\theta$  scan from a polycrystalline 180-nm-thick ScN film grown on MgO(001).

strain, and accounting for differential contraction, yields a relaxed ScN lattice constant in the range 0.4497–0.4500  $\pm 0.0005$  nm.

Typical bright- and dark-field XTEM micrographs, with a selected-area electron-diffraction (SAED) pattern, from an as-deposited ScN/MgO(001) sample are presented in Fig. 2. The ScN film thickness determined from the XTEM micrographs is 180 nm in good agreement with the expected value based upon deposition rate calibrations. From the bright-field XTEM image in Fig. 2(a) and plan-view TEM micrographs (not shown), the ScN layers have a columnar microstructure with an average column width near the film surface of  $30 \pm 5$  nm. Figure 2(a) was obtained with the electron beam oriented along the  $[100]$  zone axis of the MgO substrate. The substrate appears dark under the bright-field imaging conditions employed due to the large diffracted beam intensity. Approximately half of the ScN columns adjacent to the film/substrate interface are also of uniformly dark contrast and, during tilting experiments, retain the same contrast as the substrate. This, together with the XRD and following XTEM/SAED results, indicates that these columns grow with the orientation  $[001]_{\text{ScN}} \parallel [001]_{\text{MgO}}$ . The micrograph also reveals that the 002 columns, which have broad bases and peaked tops, are overtaken by columns with, as shown below, 111 orientation. All 002 columns terminate at distances of 5–40 nm from the substrate surface.

A corresponding SAED pattern, obtained using a  $0.4 \mu\text{m}$  diam aperture centered at the ScN/MgO interface, is shown in Fig. 2(b) and indexed in Fig. 2(c). It is composed of two superimposed aligned 100 patterns, due to ScN and MgO, with 111 ScN arcs along the film growth direction. The dis-

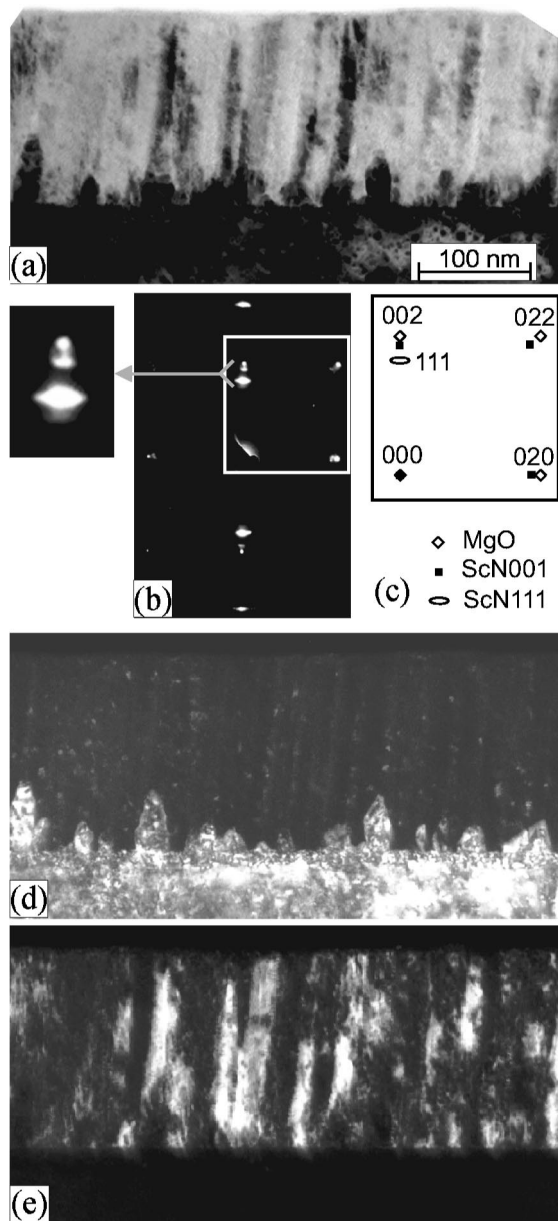


Fig. 2. (a) Bright-field XTEM micrograph, (b) a corresponding SAED pattern, (c) an indexed SAED pattern, (d) a dark-field XTEM obtained using the 020 ScN and MgO reflections in (b), and (e) a dark-field XTEM obtained using the 111 ScN reflection in (b) from a polycrystalline 180 nm thick ScN film grown on MgO(001).

crete nature of the ScN diffraction features, as opposed to polycrystalline ring patterns, reflects the strong texture in these films. The positions of the 002 MgO, 002 ScN, and 111 ScN reflections along the film growth direction correspond to interplanar spacings  $d$  of 0.21, 0.225, and 0.26 nm, respectively, consistent with  $\theta$ - $2\theta$  XRD results in Fig. 1. The ScN in-plane spacing  $d_{200}$  obtained from Fig. 2(b) is  $0.225 \pm 0.002$  nm,  $\approx d_{002}$ , indicating that 002 columns are essentially fully relaxed.

The 111 ScN diffracted intensity in Fig. 2(b) is concentrated in an arc centered along the growth direction. This shows that the 111 columns are highly oriented in the growth direction. The half-angle subtended by the 111 arcs, which

corresponds to the degree of intercolumnar misorientation in the growth direction, is  $\approx 4^\circ$ , in good agreement with XRD  $\psi$  rocking-curve measurements (see below).

The dark-field micrograph in Fig. 2(d) was obtained with the objective aperture centered on the 020 MgO and ScN reflections in Fig. 2(b) and, thus, only the substrate and the 002 set of ScN columns appear bright. The full orientational relationship between these columns, which grow in a cube-on-cube manner, and the substrate is  $(001)_{\text{ScN}} \parallel (001)_{\text{MgO}}$  with  $[010]_{\text{ScN}} \parallel [010]_{\text{MgO}}$ , for which the mismatch is  $\approx 7\%$ . The remainder of the ScN layer is illuminated [see Fig. 2(e)] when imaged in dark field using the 111 ScN reflection. Thus, during nucleation, 002- and 111-oriented islands are formed and increase in size. Following coalescence, both sets of grains grow into a columnar structure. However, the growth rate of the 111 columns is higher than that of the 002 columns and the latter set slowly die out and are overgrown by the 111 set in a kinetically limited competitive growth mode. Analyses of XTEM micrographs from several ScN layers indicate that while the initial 002 and 111 volume fractions are approximately equal, all 002 grains grow out of existence by film thickness  $t \approx 40$  nm.

The above results clearly show that the 002 islands exhibit local epitaxy with the underlying substrate. In order to investigate the in-plane orientation of the 111 grains without sampling the 002 set, we have thinned a sample from the substrate side and obtained plan-view electron-diffraction patterns orthogonal to the film surface. An example, shown in Fig. 3(a), provides evidence of a local epitaxial relationship between the 111 grain and the substrate. The primary reflections occur on (220), (422), and (440) ScN diffraction rings [see Fig. 3(b)] while the weaker reflections are due to double diffraction. All reflections are from the 111 zone axis indicating that, to within the accuracy of the measurement and consistent with the above XTEM results, all grains in the upper region of the film are oriented 111. For a sample with complete 111 texture and grains perfectly aligned azimuthally, there should be six 220 (and 440) reflections separated by  $60^\circ$  as indicated by the filled circles in Fig. 3(b). The fact that we obtain 12-fold symmetric reflection sets indicates that the 111 grains have at least two equivalent azimuthal orientations. In fact, as we demonstrate below using XRD pole figure analysis, there are four possible in-plane orientations.

Figure 4(a) is a (111) XRD pole figure, obtained with the detector angle  $2\theta$  set at  $34.415^\circ$ , from a ScN film while Fig. 4(b) is a slice of the pole figure, plotted as intensity  $I$  versus  $\psi$ , along the  $\phi=0$  axis. The central 111 peak is oriented coincident with the film growth direction and exhibits no measurable tilt. The angular distribution of the peak along  $\psi$ , which corresponds to a rocking curve, is symmetric azimuthally and has a FWHM of  $\Gamma_{111}^{111} = 3.6^\circ$ . Moving further out along the tilt direction, there are four small peaks at  $\psi = 54.7^\circ$  and  $\phi = 0^\circ, 90^\circ, 180^\circ, \text{ and } 270^\circ$  due to diffraction from the (111) planes of 002-oriented grains. These peaks correspond to the four  $\langle 111 \rangle$  directions around the  $[001]$  pole and have FWHM values of  $\Gamma_{002}^{111} = 4.8^\circ$  indicating that 002 grains have

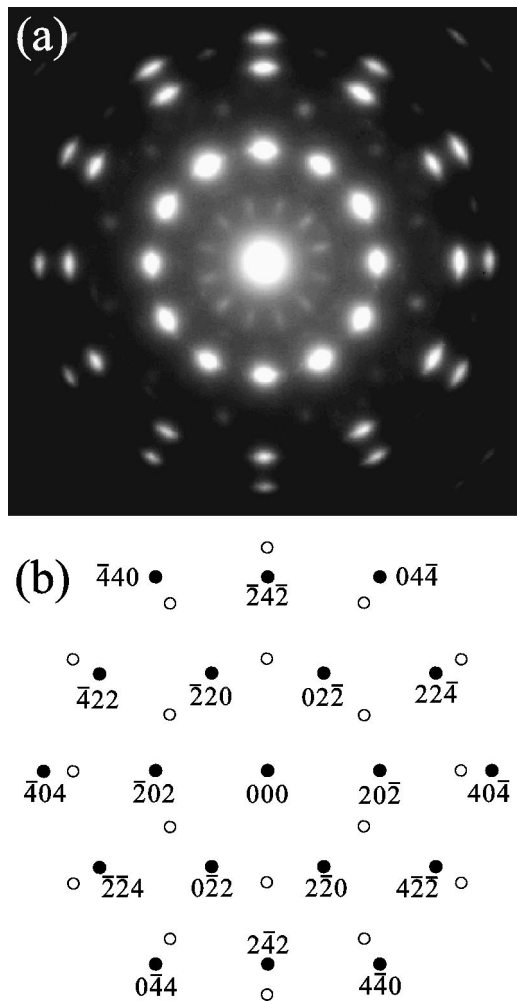


FIG. 3. Plan-view transmission electron-diffraction pattern from a polycrystalline 180 nm thick ScN film grown on MgO(001). The sample was thinned from the substrate side. (b) A simulation consisting of two [111] zone axis patterns rotated by  $30^\circ$ . The pattern denoted by solid circles is indexed.

a slightly larger average misorientation than 111 grains. If the 002 grains were randomly aligned azimuthally, the pole figure would contain a ring of intensity continuous in  $\phi$  and centered at  $\psi=54.7^\circ$ . The fact that we observe discrete peaks shows that the films exhibit in-plane preferred orientation.

The pole figure in Fig. 4(a) also contains 12 outer peaks located at  $\psi=70.5^\circ$  and separated by  $\phi=30^\circ$ . These peaks emanate from the 111-oriented grains which, in addition to their 111 texture along the growth direction, also exhibit strong in-plane preferred orientation. However, if all 111 grains were perfectly aligned azimuthally, the pole figure would contain a total of four 111 peaks: the central 111 and three peaks at  $\psi=70.5^\circ$  ( $\bar{1}11$ ,  $1\bar{1}1$  and  $11\bar{1}$ ) separated by  $\phi=120^\circ$ . The presence of twelve  $30^\circ$ -rotated peaks indicates that there are four equivalent epitaxial arrangements between the threefold symmetric (111) planes in 111 ScN grains and the fourfold MgO(001) substrate plane. The reason for this is shown schematically in Fig. 5. There are four possible directions in which two-dimensional 111 triangles can be oriented with respect to the four equivalent directions in square MgO

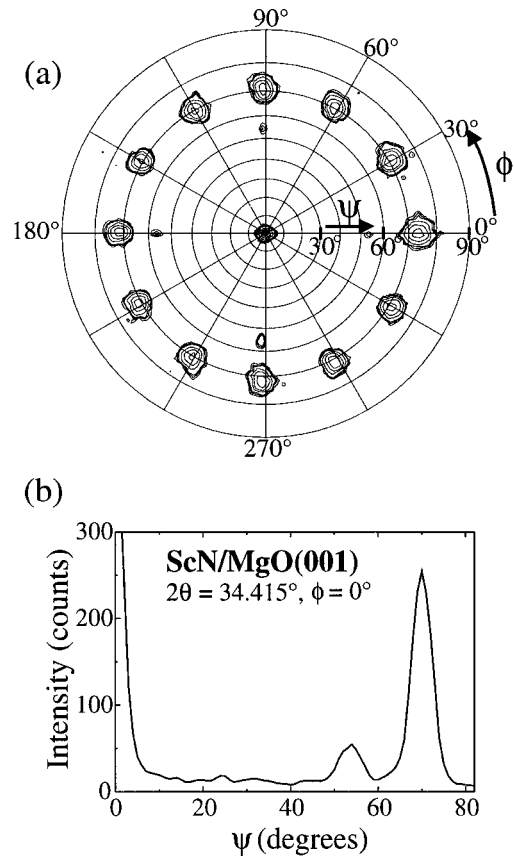


FIG. 4. (a) XRD 111 pole figure, obtained with  $2\theta=34.41^\circ$ , from a polycrystalline 180 nm thick ScN film grown on MgO(001). (b) A slice of the pole figure, plotted as intensity  $I$  vs  $\psi$ , along the  $\phi=0^\circ$  axis.

surface unit cells. Each of the four orientations leads to a set of three peaks— $\bar{1}11$ ,  $1\bar{1}1$ , and  $11\bar{1}$ —in the 111 pole figure for a total of 12 at  $\psi=70.5^\circ$ .

The above results show that 002 grains grow with a cube-on-cube local epitaxial relationship with the MgO substrate.

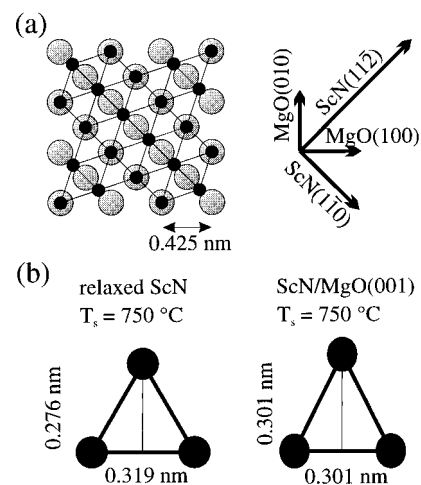


FIG. 5. (a) Schematic drawing showing interfacial atom positions for fully strained ScN(111) on MgO(001). (b) Dimensions of relaxed and fully strained triangular ScN(111) surface unit cells on MgO(001) at the film growth temperature  $750^\circ\text{C}$ .

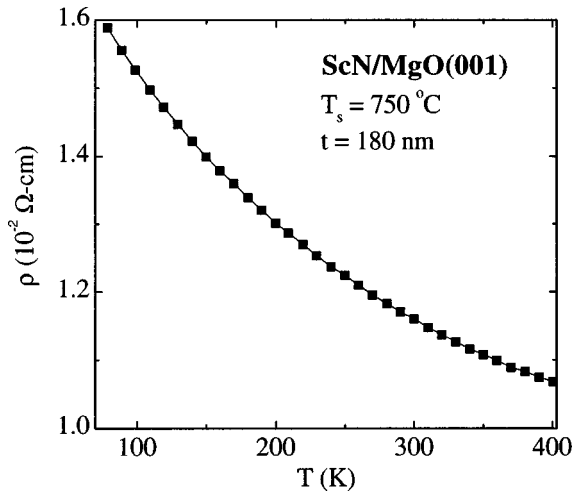


FIG. 6. Resistivity  $\rho$  of polycrystalline ScN as a function of temperature.

Using the thermal expansion coefficients from Refs. 12 and 15, together with our XRD results, yields lattice constants at the growth temperature of  $a_{\text{ScN}}(750\text{ }^\circ\text{C})=0.4513\text{ nm}$  and  $a_{\text{MgO}}(750\text{ }^\circ\text{C})=0.4252\text{ nm}$ . This corresponds to a 6% biaxial in-plane compressive strain in ScN(002), which is relaxed through the formation of misfit dislocations. In the case of 111 grains, Fig. 5(b) shows that the unrelaxed triangular building blocks of the hexagonal ScN(111) plane must lose their equilateral symmetry to grow with a local epitaxial relationship to the MgO(001) substrate. That is, ScN(111) is compressed along the  $\langle 110 \rangle$  direction by 6% and is in 9% tension in the  $\langle 112 \rangle$  direction. Following island coalescence and early stages of film growth, the 111 ScN grains relax, as shown by our XRD and SAED results.

The schematic diagrams in Fig. 5 provide a clue as to why both 111- and 002-oriented ScN grains are obtained. We assume that as in other NaCl-structure transition-metal nitrides, including TiN,<sup>18,19</sup> (002) is the lowest energy, and hence, the thermodynamically favored, equilibrium growth surface. However, within the uncertainty in bulk ScN elastic and lattice constants, the net strain energy density for 111 ScN nucleation and growth on MgO(001), due to the mixture of orthogonal in-plane tension and compression, is approximately equal to that associated with biaxially strained 002. Thus, both sets of grains are observed initially. Continued competitive growth of adjacent 002 and 111 grains, however, favors the latter due to kinetic limitations. That is, for low-temperature deposition ( $T_s=750\text{ }^\circ\text{C}$  is still only a relatively small fraction of the ScN melting point in K),<sup>20</sup> cation species landing near grain boundaries have a chance to sample relatively few sites on either grain before they find a “permanent” site and are overgrown. Under these low mobility conditions, adatoms have a larger chance of becoming trapped in the higher-energy 111 sites, and 111 grains will slowly and inexorably expand at the expense of the 002 grains as we observe in XTEM micrographs (see Fig. 2).

The room-temperature resistivity of the ScN layers was determined to be  $\rho=1.2\pm 0.1\times 10^4\text{ }\mu\Omega\text{ cm}$ , a factor of  $\approx 10^2\text{--}2\times 10^3$  larger than the range of known metallic

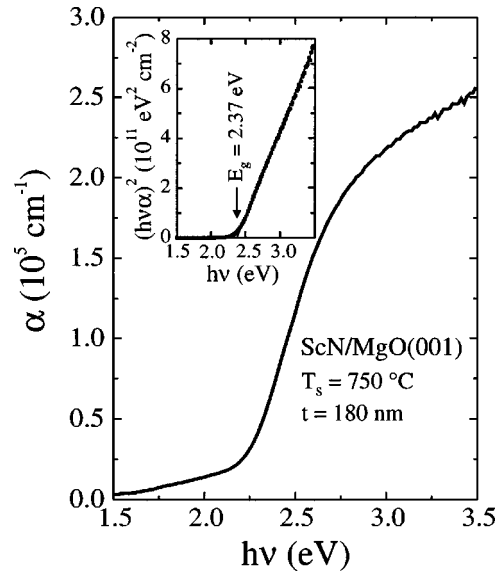


FIG. 7. The absorption coefficient  $\alpha$  vs photon energy  $h\nu$  for polycrystalline ScN. The inset is a plot of  $(\alpha h\nu)^2$  vs  $h\nu$  showing that ScN has a direct band gap with a value  $E_g=2.37\text{ eV}$  at room temperature.

transition-metal nitrides, which have resistivities from 7 (ZrN) to 130 (TaN)  $\mu\Omega\text{ cm}$ .<sup>21</sup> The resistivity of the most common metallic transition-metal nitride, TiN, is 15  $\mu\Omega\text{ cm}$ .<sup>1,2</sup> ScN resistivity versus temperature over the range from 80 to 400 K is shown in Fig. 6.  $d\rho/dT$  is negative, with  $\rho$  varying from  $1.6\times 10^4\text{ }\mu\Omega\text{ cm}$  at 80 K to  $1.1\times 10^4\text{ }\mu\Omega\text{ cm}$  at 400 K, indicative of semiconducting behavior.

Optical transmission and reflection measurements were carried out on films of different thickness  $t$  over the energy range from 1.5 to 3.5 eV. From the results, we obtained the absorption coefficient  $\alpha$  as a function of wavelength  $\lambda$  through the relationship

$$\alpha = \frac{-\ln(F)}{t}, \quad (1)$$

where  $F$  is the fraction of light transmitted through the film,

$$F(\lambda) = \frac{T(\lambda)}{1-R(\lambda)}. \quad (2)$$

$T$  and  $R$  in Eq. (2) are the measured transmittance and reflectance, respectively. The results are plotted in Fig. 7 as  $\alpha$  versus photon energy  $h\nu$ . Optical absorption is small for photon energies below 2 eV ( $\alpha < 2\times 10^4\text{ cm}^{-1}$ ), has a well-defined edge near 2.4 eV, and is large above 3 eV ( $\alpha > 2\times 10^5\text{ cm}^{-1}$ ). The large increase in absorption above the edge suggests that ScN has a direct optical bandgap. This is explicitly established by showing that the square of the product of the absorption coefficient and the photon energy is linearly related to photon energy.<sup>22</sup> Plotting  $(\alpha h\nu)^2$  versus  $h\nu$  is shown in the inset in Fig. 7 to produce a straight line whose intercept yields the bandgap  $E_g=2.37\pm 0.05\text{ eV}$ . The possibility of an additional indirect bandgap at lower energies cannot be completely ruled out due to the low absorption associated with indirect transitions.

The above analysis neglects internal reflections at the film/substrate and substrate/air interfaces. This was done due to the relatively large uncertainties in ScN refractive indices and the fact that the inclusion of these terms has no effect on  $E_g$ . It does, however, add to the uncertainty in sub-bandgap absorption coefficients as discussed below. Internal reflectivities  $R$  in weakly absorbing materials can be calculated using the relationship  $R = (n_1 - n_2)^2 / (n_1 + n_2)^2$  where  $n_1$  and  $n_2$  are the refractive indices of the upper and lower regions of the bilayer considered.  $n_{\text{MgO}}$  has been measured previously to vary from 1.70 at 0.5 eV to 1.78 at 3.1 eV,<sup>23</sup> while  $n_{\text{ScN}}$  values were determined from positions of interference maxima and minima to be  $3.5 \pm 1$ . The uncertainty in  $n_{\text{ScN}}$  is due to the broadness of the interference maxima which, in turn, results from the film thickness being approximately equal to or smaller than the optical wavelengths used in these experiments. Accounting for the  $11 \pm 5\%$  and  $7.4\%$  reflectivities at the film/substrate and substrate/air interfaces leads to an uncertainty in the absorption coefficient  $\alpha$  of  $\pm 6 \times 10^3 \text{ cm}^{-1}$  which, from the results in Fig. 6, is only significant at energies less than  $\approx 2 \text{ eV}$ .

#### IV. CONCLUSIONS

Polycrystalline NaCl-structure ScN films, 180 nm thick, were grown on MgO(001) at 750 °C by UHV magnetron sputter deposition in pure N<sub>2</sub>. The layers were columnar in microstructure with an average column size of  $30 \pm 5 \text{ nm}$  near the film surface. TEM, XTEM, and XRD pole figure analyses show that while the layers initially consisted of approximately equal volume fractions of 002- and 111-oriented grains, film texture evolved through a kinetically limited competitive growth mode, as discussed in Sec. III, to a complete 111 preferred orientation at thicknesses  $t \approx 40 \text{ nm}$ . Film/substrate orientational relationships for the two sets of grains are:  $(001)_{\text{ScN}} \parallel (001)_{\text{MgO}}$  with  $[010]_{\text{ScN}} \parallel [010]_{\text{MgO}}$  and  $(111)_{\text{ScN}} \parallel (001)_{\text{MgO}}$  with  $[1\bar{1}0]_{\text{ScN}} \parallel [1\bar{1}0]_{\text{MgO}}$  and  $[\bar{1}12]_{\text{ScN}} \parallel [110]_{\text{MgO}}$ . Thus, both sets of grains exhibited strong texture both in plane and in the growth direction. A unique component of this complex texture is that the 111 grains formed with a fourfold in-plane preferred orientation in which strained ScN two-dimensional triangular {111} unit cells meshed with square MgO unit cells.

The ScN layers have a room-temperature electrical resistivity  $\rho$  of  $1.2 \times 10^4 \mu\Omega \text{ cm}$ , which increases with decreasing temperature, indicative of semiconducting behavior.  $\rho$  ranges from  $1.1 \times 10^4 \mu\Omega \text{ cm}$  at 400 K to  $1.6 \times 10^4 \mu\Omega \text{ cm}$  at 80 K. Optical transmission and reflectivity measurements show a well-defined absorption edge corresponding to a direct band-to-band transition at  $2.37 \pm 0.05 \text{ eV}$ .

#### ACKNOWLEDGMENTS

This work was supported by the U. S. Department of Energy, Division of Materials Science, Grant No. DEFG02-96ER45439 through the University of Illinois Frederick Seitz Materials Research Laboratory, the Swedish Research Council for Engineering Sciences (TFR), and the Natural Sciences and Research Council of Canada (NSERC). The authors also appreciate the use of the facilities of the Center for Microanalysis, which is partially supported by DOE, at the University of Illinois.

- <sup>1</sup>J.-E. Sundgren, B. O. Johansson, A. Rockett, S. A. Barnett, and J. E. Greene, in *Physics and Chemistry of Protective Coatings*, edited by J. E. Greene, W. D. Sproul, and J. A. Thornton (American Institute of Physics, Series 149, New York, 1986), p. 95.
- <sup>2</sup>B. W. Karr, I. Petrov, P. Desjardins, D. G. Cahill, and J. E. Greene, *Surf. Coat. Technol.* **94/95**, 403 (1997).
- <sup>3</sup>R. Eibler, M. Dorrer, and A. Neckel, *Theor. Chim. Acta* **63**, 133 (1983).
- <sup>4</sup>A. Neckel, P. Rastl, R. Eibler, P. Weinberger, and K. Schwartz, *J. Phys. C* **9**, 579 (1976).
- <sup>5</sup>L. I. Johansson, A. Callenas, P. M. Stefan, A. N. Christensen, and K. Schwartz, *Phys. Rev. B* **24**, 1883 (1981).
- <sup>6</sup>J. P. Dismukes, W. M. Yim, J. J. Tietjen, and R. E. Novak, *RCA Rev.* **31**, 680 (1970).
- <sup>7</sup>J. P. Dismukes, W. M. Yim, and V. S. Ban, *J. Cryst. Growth* **13/14**, 365 (1972).
- <sup>8</sup>R. C. Powell, N.-E. Lee, Y.-W. Kim, and J. E. Greene, *J. Appl. Phys.* **73**, 189 (1993).
- <sup>9</sup>R. L. Doolittle, *Nucl. Instrum. Methods Phys. Res. B* **15**, 344 (1985).
- <sup>10</sup>L. J. van der Pauw, *Philips Res. Rep.* **13**, 1 (1958).
- <sup>11</sup>W. Lengauer, *Solid State Chem.* **76**, 412 (1988).
- <sup>12</sup>B. Hajek, V. Brozek, and H. DuVigneaud, *J. Less-Common Met.* **33**, 385 (1973).
- <sup>13</sup>W. Lengauer and P. Ettmayer, *J. Less-Common Met.* **168**, L7 (1991).
- <sup>14</sup>J. C. Schuster and J. Bauer, *J. Less-Common Met.* **109**, 345 (1985).
- <sup>15</sup>H. Landolt and R. Börnstein, *Numerical Data and Functional Relationships in Science and Technology, Group III*, (Springer, Berlin, 1975), Vol. 7, Pt. b1, p. 27.
- <sup>16</sup>E. Török, A. J. Perry, L. Chollot, and W. D. Sproul, *Thin Solid Films* **153**, 37 (1987).
- <sup>17</sup>J. A. Sue, *Surf. Coat. Technol.* **54/55**, 154 (1992).
- <sup>18</sup>L. Hultman, S. A. Barnett, J.-E. Sundgren, and J. E. Greene, *J. Cryst. Growth* **92**, 639 (1988).
- <sup>19</sup>L. Hultman, J.-E. Sundgren, and J. E. Greene, *J. Appl. Phys.* **66**, 536 (1989).
- <sup>20</sup>The ScN melting point is unknown, but  $>1500 \text{ °C}$  based upon XRD measurements (Ref. 13).
- <sup>21</sup>L. E. Toth, *Transition Metal Carbides and Nitrides* (Academic, New York, 1971), p. 188.
- <sup>22</sup>F. Wooten, *Optical Properties of Solids* (Academic, New York, 1972), p. 115.
- <sup>23</sup>M. A. Vidal, G. Ramírez-Flores, H. Navarro-Contreras, A. Lastras-Martínez, R. C. Powell, and J. E. Greene, *Appl. Phys. Lett.* **68**, 441 (1996).